Non-Fickian dispersion in porous media: 1. Multiscale measurements using single-well injection withdrawal tracer tests

P. Gouze,[1] T. Le Borgne,[1,2] R. Leprovost,[1] G. Lods,[1] T. Poidras,[1] and P. Pezard[1]

Received 18 June 2007; revised 20 February 2008; accepted 9 April 2008; published 28 June 2008.

[1] We present a set of single-well injection withdrawal tracer tests in a paleoreef porous reservoir displaying important small-scale heterogeneity. An improved dual-packer probe was designed to perform dirac-like tracer injection and accurate downhole automatic measurements of the tracer concentration during the recovery phase. By flushing the tracer, at constant flow rate, for increasing time duration, we can probe distinctly different reservoir volumes and test the multiscale predictability of the (non-Fickian) dispersion models. First we describe the characteristics, from microscale to meter scale, of the reservoir rock. Second, the specificity of the tracer test setup and the results obtained using two different tracers and measurement methods (salinity-conductivity and fluorescent dye–optical measurement, respectively) are presented. All the tracer tests display strongly tailed breakthrough curves (BTC) consistent with diffusion in immobile regions. Conductivity results, measured over 3 orders of magnitude only, could have been easily interpreted by the conventional mobile-immobile (MIM) diffusive mass transfer model of asymptotic log-log slope of -2. However, the fluorescent dye sensor, which allows exploring much lower concentration values, shows that a change in the log-log slope occurs at larger time with an asymptotic value of -1.5, corresponding to the double-porosity model. These results suggest that the conventional, one-slope MIM transfer rate model is too simplistic to account for the real multiscale heterogeneity of the diffusion-dominant fraction of the reservoir.

Citation: Gouze, P., T. Le Borgne, R. Leprovost, G. Lods, T. Poidras, and P. Pezard (2008), Non-Fickian dispersion in porous media: 1. Multiscale measurements using single-well injection withdrawal tracer tests, *Water Resour. Res.*, *44*, W06426, doi:10.1029/2007WR006278.

1. Introduction

[2] Modeling contaminant movement is a fundamental prerequisite to support geoenvironmental risk evaluation as well as the management and remediation of water resources. Presently, most of operational modeling tools have been constructed around the resolution of the so-called advection-dispersion equation (ADE) assuming that dispersion behaves as a diffusion-like (Fickian) process [*Adams and Gelhar*, 1992]. In this case, the mean and the variance of the contaminant (or tracer) spatial distribution scale with time (t) and $\sqrt{t}$, respectively, and the variance of the temporal distribution (i.e., of the breakthrough curve measured at a given observation spot) is finite. However, an increasing number of examples, both from situ [*Adams and Gelhar*, 1992; *Meigs and Beauheim*, 2001; *Becker and Shapiro*, 2003] and laboratory [*Silliman and Simpson*, 1987; *Berkowitz et al.*, 2000; *Levy and Berkowitz*, 2003] tracer tests, display strongly asymmetric BTCs with long tails (i.e., for times after the advective peak has passed) that appears to decrease more or less as a power law of time $C(t) \sim t^{-\alpha}$, and indicates an apparently infinite variance of the BTCs. Then, it becomes more and more certain that Fickian models fails to capture the real nature of the dispersion in natural systems submitted to common hydrological stresses; even in those thought as macroscopically homogeneous [*Levy and Berkowitz*, 2003]. In most cases, BTC analysis gives fitted values of the exponent α ranging from 1.5 and 2.5. However, it is generally difficult to measure accurately the BTC power law slope. Indeed, in the vicinity of the main concentration peak, measured concentration may be corrupted by the transition from the Fickian concentration decrease to the rate-limited decrease. Then, as concentration decreases toward very low values, measurement inaccuracy may spoil the estimate of the slope. Finally, it is difficult to evaluate if the observed BTC tail represents effectively the asymptotic behavior of the tracer recovery or a transitional behavior. To tackle the asymptotic non-Fickian dispersion behavior, high-resolution sensors and long-lasting recording of the tracer recovery are required.

[3] Non-Fickian dispersion properties, their origin and their relation to the geological heterogeneity are still debated. Authors have explored different approaches for better capturing the processes that control non-Fickian dispersion. Non-Fickian dispersion may be the result of long-range

[1] Géosciences, UMR 5243, Université de Montpellier 2, CNRS, Montpellier, France.
[2] Now at Géosciences Rennes, UMR 6118, Université de Rennes 1, CNRS, Rennes, France.

0043-1397/08/2007WR006278$09.00

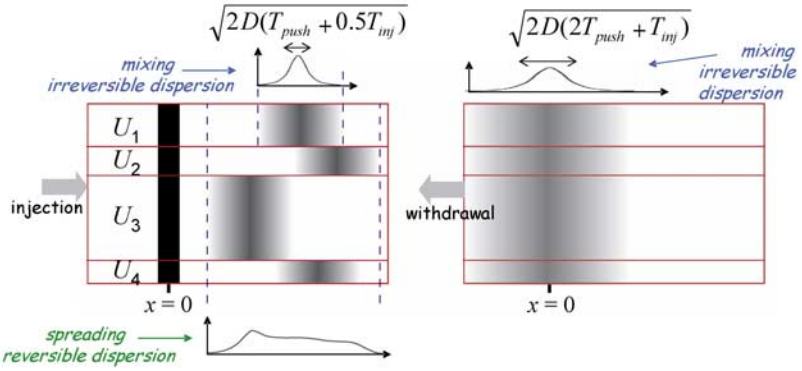

Figure 1. Schematic representation of the reversible-irreversible dispersion. SWIW tracer tests act to cancel long-range velocity correlations. Gray zones denote the concentration distribution (left) at the end of the push duration ($t = T_{push} + 1/2\ T_{inj}$) and (right) when the tracer mass center is back to the initial position at time $t = 2T_{push} + T_{inj}$. The black zone on the left corresponds to the tracer at the initial time ($t = 0$).

spatial correlation of geological structures and permeability. Multichannel model, in which all the velocities are infinitely correlated is the end-member case of this class model [*Becker and Shapiro*, 2003; *Gylling et al.*, 1999]. The overall mass transport is the sum of elementary transport in channels of distinctly different properties (leading to different flow rate and residence time), each of the channels being independent from each others. With this model, it is possible to reproduce power law-tailed BTC, by choosing the appropriate distribution of channel properties. Yet, recent results obtained by *Becker and Shapiro* [2003] when analyzing both well-to-well and single-well injection withdrawal tracing experiments show that the scaling of the residence time distribution is strongly controlled by the boundary condition (either prescribed flow rate or prescribed pressure) at the injection point and by flow geometry. The existence of long-range spatial correlation is also the basic assumption in models that describe dispersion as the result of alpha-normal (Levy flight) velocity distribution [*Benson et al.*, 2001], although quantitative relation between alpha-normal velocity distribution and the effective velocity correlation is not straightforward [*Le Borgne et al.*, 2007].

[4] Alternatively, non-Fickian dispersion may be represented by long-range temporal correlations of the solute motion that may be due to mass transfers in small-scale geological structures. For instance, the mobile-immobile mass transfer (MIM) model assumes mass exchanges between the moving fluid and a less permeable domain in which fluid is considered as immobile [*Haggerty and Gorelick*, 1995; *Carrera et al.*, 1998; *Haggerty et al.*, 2000]. The discrimination between the effects of spatial correlations controlled by large-scale structures and temporal correlations controlled by small-scale structures, both leading to non-Fickian transport, is a difficult task because it is most probable that both may be present simultaneously in some heterogeneous reservoirs. Nevertheless, it is possible to minimize velocity spatial correlation by performing single-well injection withdrawal (SWIW) tracing experiments and selecting reservoir targets displaying large-scale homogeneity.

[5] SWIW tracing tests, also called push-pull or echo tracer tests, consist in injecting a given mass of tracer in the medium and reversing flow after a certain time in order to measure the tracer breakthrough curve at the injection point [*Gelhar and Collins*, 1971, *Tsang*, 1995, *Haggerty et al.*, 2001, *Khrapitchev and Callaghan*, 2003]. This technique presents several advantages. First, the reversal of flow warrants an optimal tracer mass recovery. Second, SWIW tracer test allows measuring the irreversible dispersion (or mixing) whereas reversible dispersion; that is, the spreading due to long-range correlated path, taking place during the tracer push phase is canceled during the withdrawal phase [*Becker and Shapiro*, 2003, *Khrapitchev and Callaghan*, 2003]. The quantification of the reversible and irreversible dispersion refers to a given scale of observation which, in our case, is the maximal distance moved by the tracer during the SWIW tracer test. More precisely, velocity correlation, over distance smaller than the exploration size will result in irreversible dispersion (diffusion and mixing) whereas adjective spreading due to velocity correlation larger than the exploration size will be canceled (Figure 1). Thus, the measured dispersion using SWIW tests is only caused by tracer molecules that do not follow the same path on the injection and the withdrawal phases. Third, using SWIW tests, tracer may be pushed at different distances from the injection point, thus visiting different volumes of the system using a single well. This latter aspect, which was barely investigated in previous studies, allows exploring the dispersion processes for increasing volumes of reservoir, and testing, and subsequently validating, the predictive nature of the models.

[6] A set of SWIW tracer tests is presented in this paper. Our objective was to obtain high-quality measurements to explore the asymptotic behavior of this type of mass transfers and to investigate the scale effect on dispersion. For this first set of experiments, the intention was to focus on the study of the diffusion processes in immobile zones (i.e., matrix diffusion). Consequently, we intentionally targeted an aquifer displaying large-scale homogeneity (i.e., no fractures or large range correlated permeability zones), but small-scale heterogeneity. A second requirement was to minimize regional flow that may invalidate the radial symmetry assumption. For that seawater intrusion zones are ideal, because of the relative motionlessness due to the

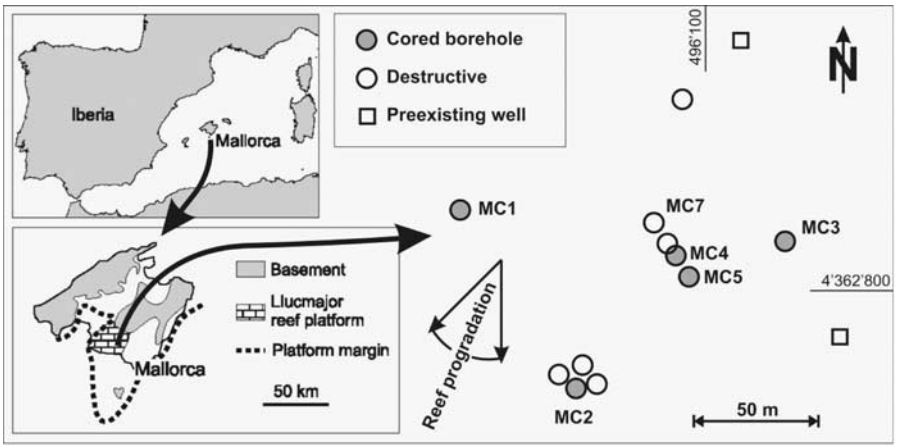

Figure 2. Situation map of the Ses Sitjoles test site. SWIW tracing experiments reported in this paper concern the MC2 borehole (modified from *Jaeggi* [2006]).

strong hydrostatic constraints imposed by the water layering configuration.

[7] The purpose of this paper is to describe the tracing experiments, compare them to previously published data and discuss the results in the frame of non-Fickian dispersion. First, the test site and the rock properties are presented in section 2. The experimental setup, together with the description of the new equipment and methodology developed for this purpose are presented in section 3. In section 4, the set of SWIW tracer tests is presented and results are discussed and tentatively modeled by the classical MIM mass transfer model. Finally, summary and conclusions are given in section 5. In a companion paper [*Le Borgne and Gouze*, 2008], an improved MIM mass transfer model is explored using a continuous time random walk model explaining the observations at large scales.

2. Site Location and Reservoir Properties

2.1. The Ses Sitjoles Test Site

[8] The Ses Sitjoles experimental site was developed in 2002–2005 as part of the European Advanced Logging Investigations in Coastal Environments (ALIANCE) network of experimental sites. The prerequisite, when developing this site, were twofold: (1) a high-porosity porous aquifer displaying less heterogeneity as possible in order to study flow and transport in simple, but natural, structures, and (2) a very low regional flow as required to validate the radial approximation imposed by single-well tracer tests. As it will be explained below these requirements are meet at the Ses Sitjoles test site. This site is situated 6 km inland at about 50km south from the city of Palma de Majorca, Balearic Islands (Figure 2). The Ses Sitjoles idropad is a set of eleven 100 m deep boreholes separated by distances ranging from 2.5 m to 100 m in a zone where the seawater intrusion is well developed (e.g., the salt intrusion have been measured at more than 20 km inland in the area of Palma). At the site location, the salt intrusion is measured at a depth of 78 m with a transition from continental water to seawater (salinity 36 g L^{-1}) of 16 m. From depth 78 m to the bottom of the boreholes (100 m) pore fluid is seawater with only weak composition variation with depth (Figure 3). The relatively high salinity of the continental water (salinity 5 g L^{-1}) in this area is due to the massive use of the aquifer for irrigation that creates locally seawater upconing and leaching of the salt residues due the close proximity of the sea.

[9] Regional flow in the continental water zone is intense in karstic features that take place in the first two meters below the water table. Caves as large as 2 m diameters have been observed in some of the boreholes of the test site. This large transmissivity of the upper part of the aquifer is largely exploited for crop irrigation and tourism, albeit the increasing salinization of the aquifer, resulting from local overexploitation and decreasing meteorological recharge, becomes a serious problem. The intense flow in the upper part of the aquifer is easily visible on the temperature gradient which almost null (Figure 3). In contrast, natural flows in the transition zone and in the sea intrusion are lower than our measurement capabilities and can be adequately considered as null over the duration of the tracing experiments. For this reason this site is well adapted for tracing experiment and especially SWIW tracing experiments for which regional flow can corrupt strongly the results without any simple possibility of applying efficient corrections. Below the transition zone, seawater is close to thermodynamic equilibrium with respect to the rock forming assemblage (almost pure calcite and dolomite) which corroborates the large residence time of this fluid in the aquifer. In the transition zone chemical disequilibrium produces mass transfers with locally dissolution or precipitation features (depending on the mixing ratio), that can be observed on samples and on the pH profile (Figure 3). This configuration is observed in most of the seawater intrusion in coastal aquifers.

2.2. Porosity and Permeability

[10] The tracer tests presented here are performed at a depth of 94 m (i.e., more than 30 m below the saline wedge top) in the cored well MC2. In this zone, rocks belong to the reef distal slope and are visually quite homogeneous. This apparent homogeneity at meter to decameter scale can be well observed on the Capo Blanc sea cliff which offer us a unique opportunity of following the entire reef sequences, and also on the core extracted from the different wells of the site. This homogeneity can be evaluated also from the acoustic velocity and the bulk electrical conductivity profiles. The compression wave velocity (V_p) and the formation

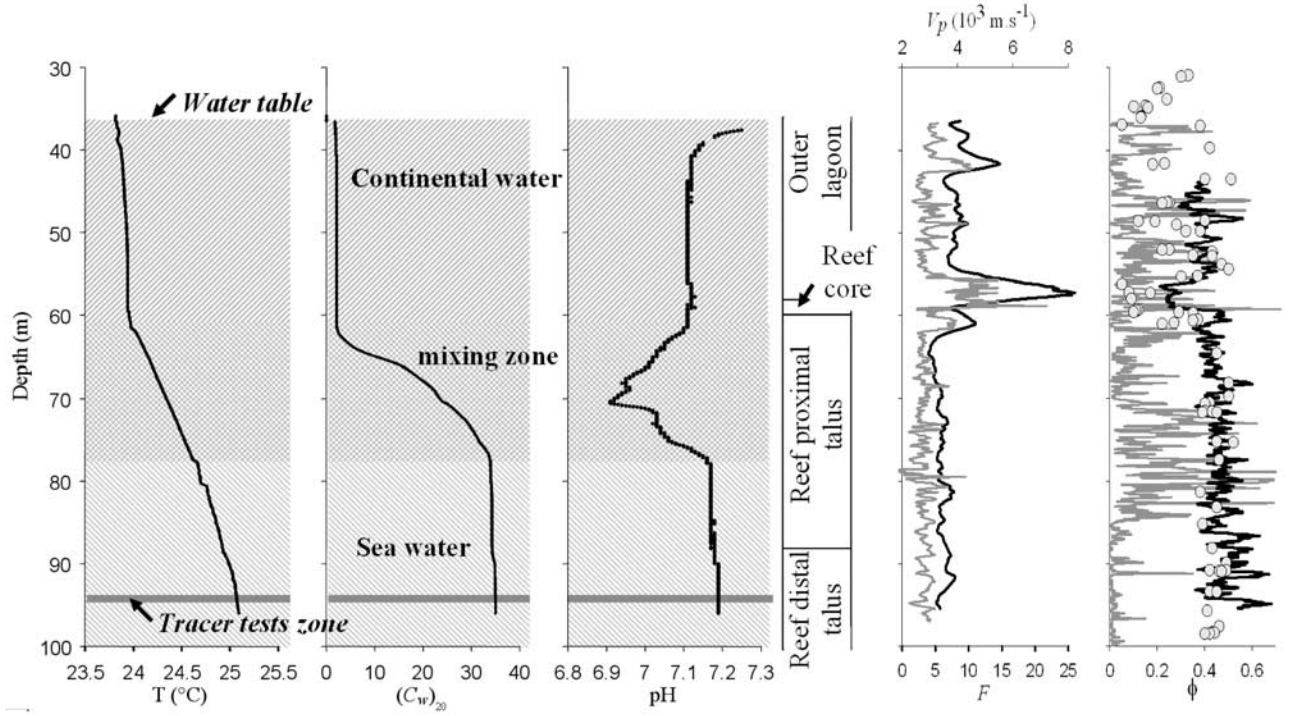

Figure 3. Fluid and rock property profile versus depth in MC2 borehole. From left to right: fluid temperature T; equivalent fluid electrical conductivity in mS cm^{-1} at 20°C $(C_w)_{20}$; fluid pH; acoustic velocity V_p; formation factor F deduced from the bulk electrical resistivity log; and porosity ϕ obtained by processing acoustic images of the well walls noted ϕ_{macro} in the text (gray curve), measured using neutron probe (black curve), and measured by the triple-weight method on core samples (circles).

factor $F = C_w/C_b$, where C_w and C_b are the electrical conductivity of the pore water and of the bulk rock, respectively, are displayed in Figure 3.

[11] The porosity of this part of the reef has been measured on several samples in well MC2 and in the other wells around. Porosity deduced from Hg porosimetry and triple-weighting technique (using 2 to 10 cm^3 massive rock samples) range from 40% and 49% in this zone (depth 88 m to 96 m in MC2). In the zone delimited by the measurement chamber (centered at 94 m), the total porosity measured on plugs ranges from 42 to 45% (Figure 3), whereas the effective porosity deduced from throughout tracing experiments on a 720 mm length cores (diameter 90 mm) is 28% telling us that a noticeable part of the porosity does not

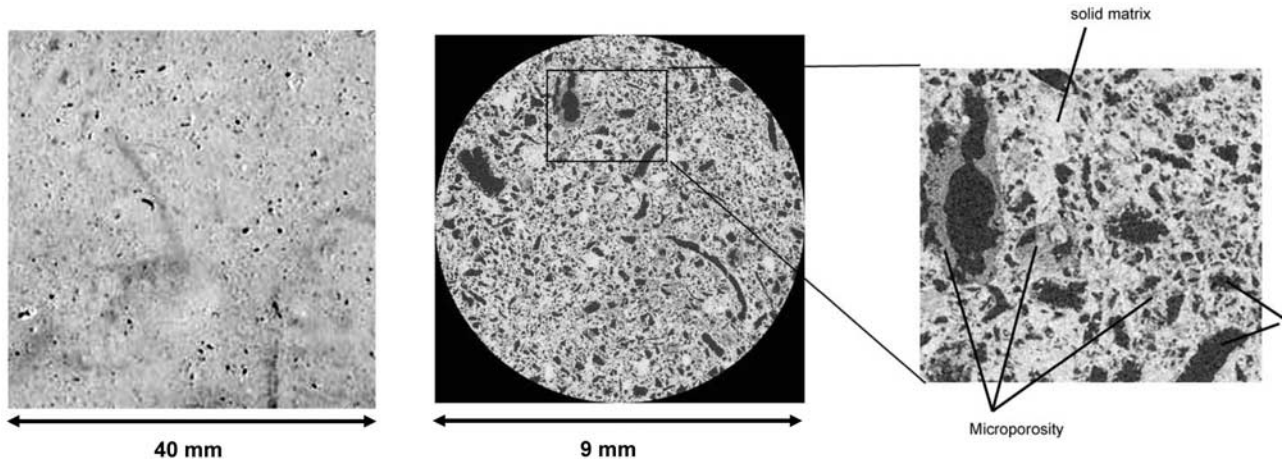

Figure 4. Illustration of the mesoscale structural heterogeneity (borehole MC2, depth 94 m). (left) Photograph of sawn surface. (right) Numerical cross section in a microtomographic image of a 9 mm diameter sample; pixel size is 5.4 μm. Gray levels denote the X-ray absorption. For a single rock-forming mineral (here rock is almost 100% pure calcite) X-ray absorption is linearly proportional to the porosity. The voids appear in black, the solid matrix appears in white, and the gray levels represent the fraction of pores of sizes less than the pixel size (i.e., the microporosity).

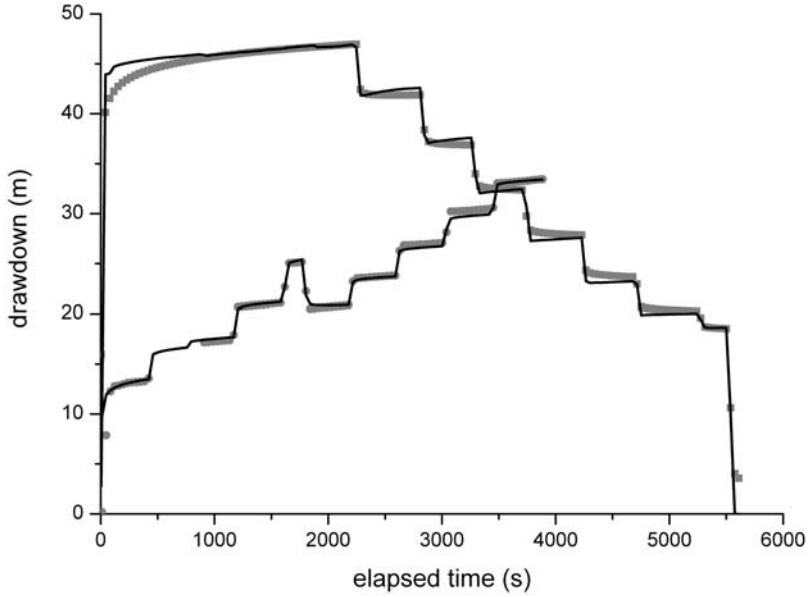

Figure 5. Step drawdown test results in the interval 93.55–94.35 m, with flow rates ranging between 1.113 $m^3 s^{-1}$ and 3.073 m^3. Dotted curves are measured data and continuous curves are outputs from the fitted model (transmissivity = 1.6 $m^2 s^{-1}$).

belong to the mobile (advective) domain. The connected porosity was also evaluated from analyzing X-ray microtomography images (resolution 5.4 μm, Figure 4) of small plugs of 9 mm diameter. This approach allows the discrimination between connected and nonconnected porosity [*Noiriel et al.*, 2005]. Connected porosity evaluated this way ranges from 27 to 30%, (total porosity from 32 to 36%) but it must be stated here that the samples were chosen to contain no visible macropores (i.e., pores larger than 1 mm). Nevertheless, the ratio of the effective porosity to the total porosity appears coherent with measurements performed on larger size samples. The observation of the borehole cores (diameter 90 mm) shows that locally enhanced porosity zones exist because of fossil accumulations and bigger coral fragments, but these features represent a very small fraction of the reservoir volume at the depth of the experiment. This can be seen also on the macroporosity (ϕ_{macro}) profile obtained from the acoustic well wall imagery. This measure integrates the cross-sectioned macropores larger than about 10 mm^2. The profile displayed in Figure 3 shows that at depth 94m ϕ_{macro} is smaller than 3% and should not modify the meter-scale permeability, neither forming long-range channels.

[12] The presently observed porosity is not the primary porosity, because the system has followed a complex diagenic history [*Pomar and Ward*, 1999]. The $\delta^{18}O$ values are negative ($\delta^{18}O \approx -4‰$) in MC2. These negative values are typical of a diagenesis from groundwater of meteoric origin. However, as the initial porous medium had a high porosity and was quite homogeneous at meter to decameter scale (typical from reef talus), diagenesis was probably homogeneously distributed. As a result, the actual porosity remains quite homogeneous. Studies at larger scale, including classical geophysical logging (for example using sonic propagation) and well wall imaging (optical and acoustical), shows that the spatial changes in porosity follow the sequences of subhorizontal sigmoidal progradation lens resulting from the growth of the distal talus reef platform. Porosity variations are typically occurring over vertical distances of five to ten meters, and tens to hundred meters horizontally. For a more complete description of the aquifer petrologic properties at large scale, the reader can refer to *Jaeggi* [2006]. The high-porosity porous media ensures a large connectivity of the pore and throats and the existence of a single connected void cluster and few long-distance dead head paths. Albeit it is difficult to measure these parameters at meter scale, the analysis of the X-ray tomographic images on several centimeter-scale samples shows the existence of a single connected void cluster with few to no centimeter-scale dead end structures.

[13] Permeability was measured from pumping test before and during the tracing experiments using the same configuration (i.e., in between two packers at depth 94 m). Examples of drawdown curves for step withdrawal and injection tests are reported in Figure 5. Data are analyzed assuming cylindrical flow. We use the model of *Lods and Gouze* [2004] which includes pumping well storage and skin effects. The obtained permeability values are around 1.9×10^{-12} m^2. Measurements on cores (length 500 mm diameter 90 mm) sampled at depth 90 to 94 m range from 0.4×10^{-13} to 2.5×10^{-13} m^2. Permeability was also measured on plugs (2.5 cm diameter, 5 cm length. Seven measurements from depth 88m to 96m in MC2 give values ranging from 0.2×10^{-13} to 1×10^{-13} m^2. Finally, the permeability tensor was obtained by the calculation of the Stokes equations from meshing the XMT images [*Bernard et al.*, 2005] giving a permeability ranging from 0.11×10^{-12} to 0.17×10^{-12} m^2. These measures, made at different scales, show that scale effects on the permeability are very low from pore scale to decimeter scale, and moderate (1 order of magnitude) from decimeter to decameter scale. This is consistent with the homogeneity of many physical parameters measured by conventional logging.

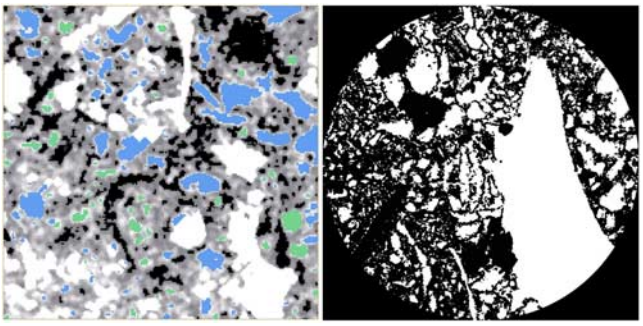

Figure 6. Illustration of the microscale structural heterogeneity (borehole MC2, depth 94 m). (left) Numerical cross section in a microtomographic 3-D image (pixel size 5.4 μm; the size of the displayed area is 3 mm $\times$ 3 mm). Data have been processed in order to individualize the solid rock (in black); the connected porosity, i.e., the mobile domain (in white); the microporosity (gray scale); the dead ends fraction of the macroporosity (in blue); and the trapped porosity (green). (right) Numerical binary cross section in a microtomographic 3-D image (pixel size 1.2 μm; the size of the image is 2 mm $\times$ 2 mm). Black denotes solid calcite and white denotes voids. The structure of the microporosity is distinctly visible.

2.3. Pore-Scale Heterogeneity

[14] The fundament of the MIM mass transfer model is to account for the mass exchanges between the moving fluid and the zones where the fluid is assumed to be immobile (the matrix). MIM model assumes that solutes may be trapped in immobile zones from which they are slowly released by diffusion [*Haggerty and Gorelick*, 1995; *Carrera et al.*, 1998; *Haggerty et al.*, 2000]. It follows that large residence times are expected in the immobile domain because of mass transfers controlled by diffusion, which are at the origin of long-lasting tails of the BTCs [e.g., *Haggerty et al.*, 2001]. Subsequently, it must be assumed that porous media is structurally bimodal with a mobile domain where advection is dominant and an immobile domain where mass transfers are diffusion-dominant. Some parts of the porous media, such as dead ends and trapped pores are clearly immobile, whereas others, such as intergrain porosity, may be assumed immobile as soon as permeability is very low compared to the main permeable structure of the rock (see review by *Haggerty and Gorelick* [1995]). The contribution of the immobile domain to the change in the mobile concentration is modeled by linear mass exchange processes which are embedded in a sink-source term in the advection-dispersion equation. This sink-source term can be expressed by a convolution product of a time-dependent function, called memory function, and the time variation of the mobile concentration (see section 4.4). The memory function depends on the properties of the immobile domain only, and therefore it is an intrinsic characteristic of the diffusivity pattern of the immobile domain and of its accessibility to the solute moving in mobile domain. Then, in the frame of the MIM mass transfer model, pore-scale heterogeneity of the mobile domain and pore-scale heterogeneity of the immobile domain must be distinguished. The characteristic of the macropores cluster forming the mobile domain will control macroscopic dispersion whereas dead-end macropores and microporosity will control diffusion in the immobile domain.

[15] Both macropores and microscale structures can be accurately imaged using X-ray microtomography (XMT). XMT is a noninvasive 3-D radiographic technique based on the specific X-rays attenuation of the different component (i.e., minerals and void) of the rock. The absorption maps can be related directly to the chemical composition of the rock (attenuation increases with the atomic mass) and its bulk density. Here, the rock is pure calcite and the X-ray absorption computed in each of the voxel is simply proportional to the fraction of calcite present in the voxel volume, i.e., inversely proportional to the porosity. Figures 4 and 6 displays XMT numerical cross sections of 1 cm diameter core sampled at the depth of the tracing experiments. Using an optical bench tuned to obtain 5.4 μm size voxels, one may clearly observe the complexity of the structure macropores structures (Figure 4). At this scale, the absorption histogram of the 3-D images ($\sim 2048^3$ voxels) displays 3 peaks that correspond to the pores (low X-ray absorption), the massive rock (the higher absorption) and an intermediary phase which can be assigned to microporous rock. After being segmented in these three phases (i.e., macropores, microporosity and solid), specific algorithms, can be implemented to extract the closed (unconnected) pores within the microporous phase, the closed pores within the solid phase, the connected pore cluster, and its dead ends branches. The connected pore cluster forms the mobile domain, whereas the microporous phase, the closed pores within the microporous phase and the dead end clusters form the immobile domain. The extent of the immobile domain can be seen in Figure 6. Diffusion in dead end clusters and closed pores is controlled by the molecular diffusion of the tracer in water only, whereas bulk diffusion of the tracer in the microporous phase depends as well on its intrinsic properties, i.e., porosity, tortuosity, constrictivity. The porosity of the microporous phase is directly given by the X-ray absorption, but the determination of the others microstructural parameters require using higher-resolution setup. For a resolution of 1.4 μm, the absorption histogram is clearly bimodal, and it can be assumed that the void-rock structure is well pictured (Figure 6). At all scales, connected pore structure appears very tortuous with high variation of the constrictivity, and high proportion of dead ends promoting slow flow paths where diffusion is certainly dominant. Thus, the occurrence of important MIM mass transfers is expected.

[16] Because of the high porosity and permeability of this aquifer, the low-scale dependence of these parameters at infradecameter scales, and the apparent structural complexity of the pore network and matrix structure, this test site is perfectly appropriate to investigate non-Fickian dispersion processes due to diffusion processes in the water immobile part of the aquifer.

3. Experimental Setup

[17] The SWIW tracer tests performed at the Ses Sitjoles experimental site consist in injecting a tracer pulse (duration T_{inj}), flushing it with water (duration T_{push}), and then pumping it back at the same flow rate until the tracer concentration become lower than the sensor resolution (Figure 7). The equipment built to perform SWIW tracer tests includes a dual-packer system delimiting an injection

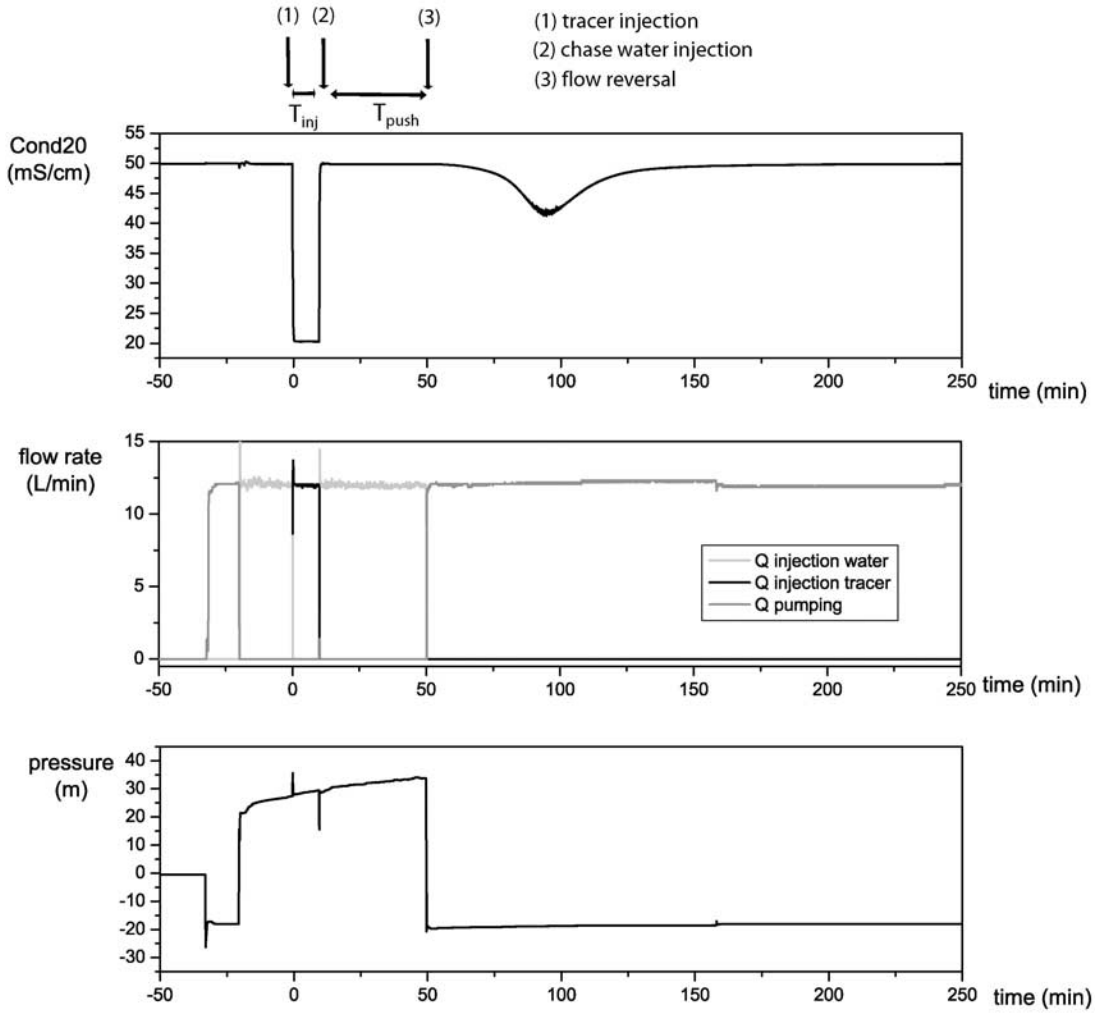

Figure 7. Example of SWIWT monitoring (tracer test 1–1). Evolution of (top) conductivity, (middle) flow rates, and (bottom) pressure as a function of time. The experiment was performed at 94 m depth. The tracer injection time is T_{inj} = 600 s and the flushing water injection duration is T_{push} = 2400 s. The flow rate is 2×10^{-4} m^3 s^{-1} (i.e., 12 L min^{-1}). The resident water conductivity is approximately 50 mS/cm.

zone of 0.675 m long. The downhole system is designed to minimize the volume of the pumping chamber, which is here less than five liters (including the annulus between the tool and the well wall), in order to reduce mixing in the system. The design is optimized to reduce potential immobile zone in the measurement chamber. Pressure sensors are fitted above the upper packer, below the lower packer and in the pumping chamber, which is equipped for receiving specific measurement probes including conductivity, pH, fluorescent dye or ion specific sensors. Data streams are multiplexed downhole together with additional data, such as the fluid temperature, the temperature of electronic equipment and the pressure of the downhole pumping system. Digitalized data are transmitted to the surface via a standard logging four-core cable and then multiplexed with the surface parameters, i.e., the flow rate and the pressure of the tracer injection hydraulic line, of the water flush injection line and of the withdrawal line. Each of these hydraulic lines is equipped with a dedicated pumping system made of 2 to 3 serial-assembled pumps, allowing controlling the flow rate by tuning the pump frequency. The withdrawal pump system is in the downhole equipment whereas the injection (tracer and flushing water) pumping system is in the surface equipment. Details of the downhole and surface equipment are given in Figure 8. Switching from each of the line (e.g., from tracer injection to water flush injection) is operated downhole in the hydraulic chamber by a slide valve. This system allows performing sharp rectangular pulse injection of duration (T_{inj} as short as 120 s. Assuming radial cylindrical geometry the maximum advection distance of the tracer plume is

$$x \cong \left((QT/2H\pi\phi_m) + r_w^2\right)^{1/2} - r_w,$$

where Q is the injection rate, H the height of the pumping chamber (0.675 m), $T = T_{push} + 0.5T_{inj}$ with T_{push} the push duration, ϕ_m is the porosity of the mobile domain and r_w is the well radius (here 0.056 m). With ϕ_m = 0.35, T_{push} = 7200 s, T_{inj} = 300 s and $Q = 2 \times 10^{-4}$ m^3 s^{-1} the maximum advection distance of the tracer is about one meter and the volume of aquifer visited by the center of mass of the tracer is QT/ϕ_m = 4.2 m^3. The estimated maximum investigation

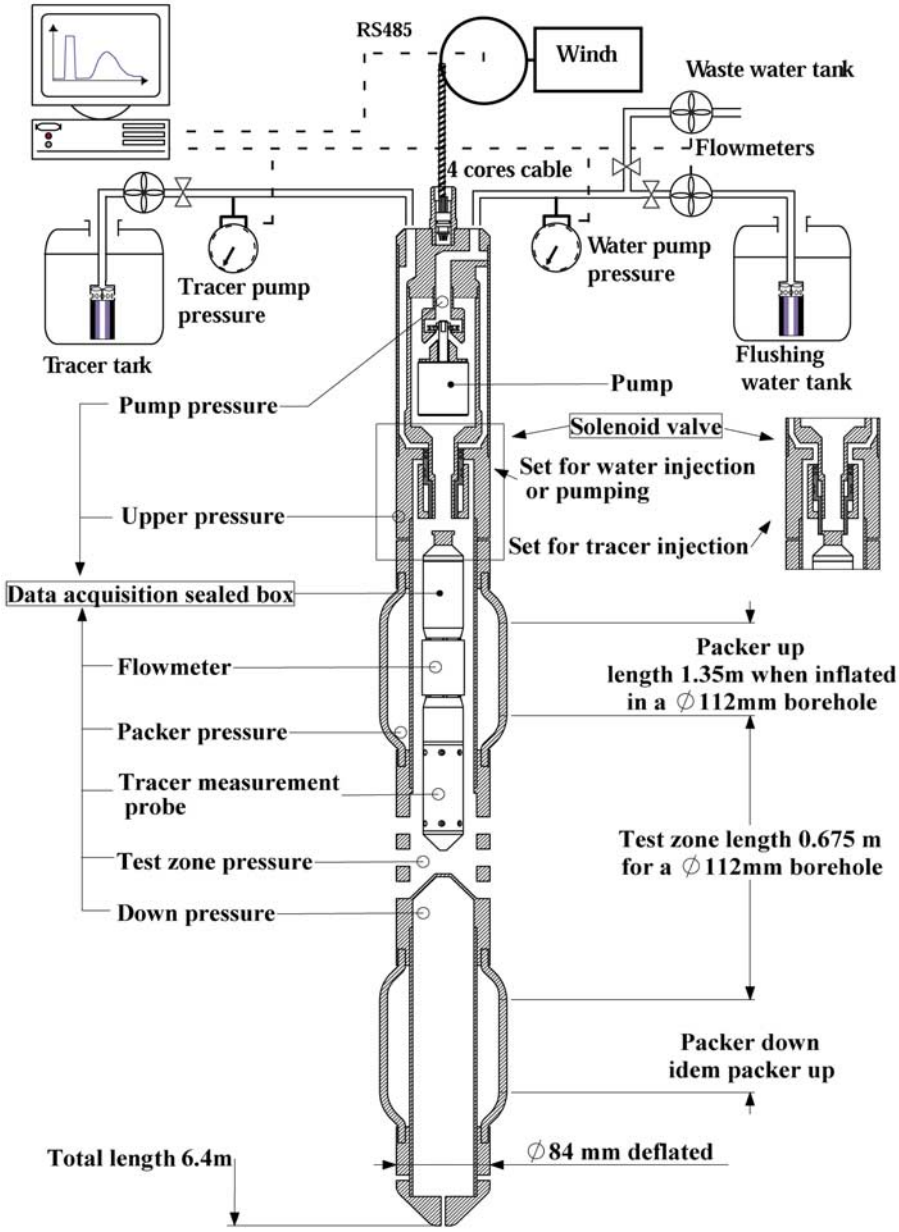

Figure 8. Schematic of the downhole probe and the surface equipment.

distance and volume is 2.8 m and 39 m^3, respectively for T_{push} = 67500 s (experiment number 1–6).

[18] We are interested here in studying the behavior of nonreactive tracers (i.e., tracers that do not react with the rock fraction of aquifer). It is then important to be sure that no sorption takes place in the system. For that, each of the experiment was performed twice with identical experimental conditions using two distinctly different tracers. In the first experimental run, the tracer is the salty water previously extracted from the borehole, then partially diluted with lower-salinity water pumped from the same borehole at lower depth (in the transition zone above the seawater intrusion). The main advantage of using weakly diluted solution of the in situ fluid is to reduce to null the occurrence of sorption on the rock in which all the sorption sites are already saturated. However, there are two drawbacks with this method. First, the resolution of the conductivity sensors (Hydronaut Ocean Seven 304), placed in the pumping chamber in between the two packers, allows measurement over less than 3 orders of magnitude, which is insufficient to tackle power law tails on BTC. Second, dispersion effects due to density differences between the tracer and the in situ fluid may occur [*Tenchine and Gouze*, 2005]. Indeed, the density difference between the tracer fluid (low-salinity fluid) and the resident water (seawater) is relatively large (see Table 1). To detect potential macroscopic movement of the tracer plume by density, the vertical position of a volume (0.5 m^3) of continental water injected in between two inflatable packers was monitored during 96 h using an induction tool positioned in the well at the exact depth of the injection (Figure 9). The induction tool measures the bulk formation resistivity (rock and water) averaged over about 1 m^3 of rock. The initial conductivity difference between the two fluids is 4700 mS m^{-1}. Figure 9

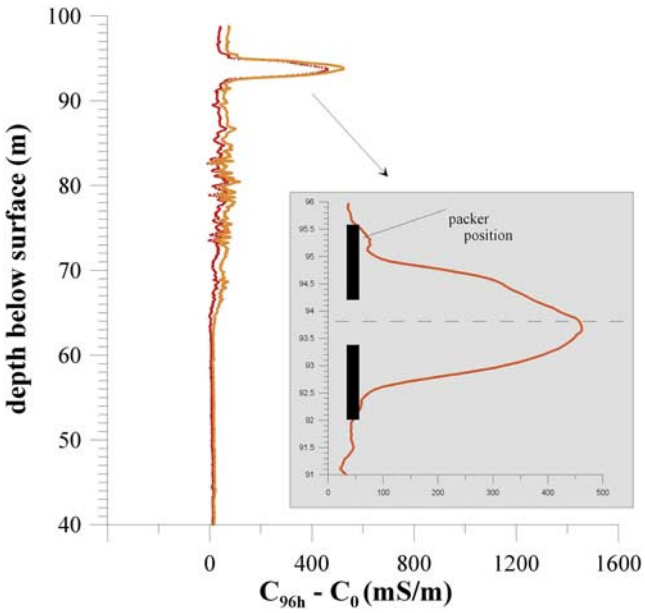

Figure 9. Difference between induction log in natural conditions (C_0) and induction log 96 h after the injection of 3 m^3 of freshwater between packers at 94 m in well MC2. The difference is shown as a function of depth for both the short- and long-range induction logs. The positive anomaly at 94 m marks out the location of the injected plume of freshwater 96 h after injection.

displays the difference between the induction conductivity profile in natural condition (i.e., before the injection) and the induction conductivity profile performed 96 h after the continental water injection. The difference between the mass center of the low-salinity plume with the packer position axis appears to be minor over the timescale of the experiments. Furthermore, we performed several SWIW tracing experiments with the same setup but with different salt concentration (conductivity difference ranging from about 760 to 3580 mS m^{-1}). Only small differences in the BTC shape, without any ubiquitous correlation with the initial tracer concentration, are observed.

[19] For the second experimental run, we use a solution of 1 ppm mass of 99% pure uranine (fluorescent dye) diluted in the formation water previously extracted from the borehole. Previous laboratory tests showed that this compound is stable in seawater at least for the timescale required in the field experiments. More precisely, calibrated concentrations as low as 10 ppt uranine in seawater have been repetitively measured as constant during several weeks. The objective, using this type of tracer, is to perform measurements over more than 5 orders of magnitude of concentration. A specific high-resolution sensor, called TeLog, was developed for this purpose. In TeLog, uranine fluorescence and turbidity are measured using a set of short-range band-pass filters and a high-sensibility photomultiplier with a computer assisted adjustable gain system. An averaged value over 30 samples (and its standard deviation) is recorded every 9 s together with a similar average of the dark signal (i.e., the noise of the photomultiplier) which was proved to be always lower than few ppt. Preexperiment and postexperiment calibration were performed, showing that reproducibility is better than few tens of ppt without any further correction. Figure 10 displays the calibration curves as it is measured in laboratory using a set of reference solutions for which dilution procedure (using the same diluted seawater) was controlled a posteriori by spectrometry measurement using a SHIMADZU RF 5301PC spectrofluorometer. Figure 10 shows also an example of recovery curve displaying the calibrated response for each gain. The concentration curve is perfectly continuous over all the range of measurement. The TeLog probe, which has exactly the same geometry than the conductivity probe, was placed similarly in the pumping chamber between the two packers.

[20] A comparison example of BTC using salinity and uranine as tracer is given in Figure 11. Results using these two tracers are very similar. Combining the properties of the two tracers, it can be inferred that neither noticeable density effects using low-conductivity water as tracer nor sorption effects using uranine are measured.

4. SWIW Test Results and Discussion

4.1. Breakthrough Curves for Tracers 1 and 2

[21] Different tracer tests were performed by pushing the tracer at different distances from the injection well, before pumping it back to the well (Table 1). Figure 12 presents the obtained BTC for different injection durations using tracer 1 and tracer 2 (conductivity and optical measurement, respectively).

Table 1. Experiment Catalog[a]

Test Number	Tracer Pulse Duration T_{inj}[b]	Injection Duration T_{push}[b]	Initial Concentration C_0	Figure
1–0	600 (10)	1,200 (40)	2020 mS m^{-1}	Figure 12
1–1	600 (10)	2,400 (40)	2020 mS m^{-1}	Figure 11
1–2	240 (4)	2,400 (40)	2030 mS m^{-1}	Figure 11
1–3	600 (10)	2,400 (40)	2020 mS m^{-1}	Figure 11 and 12
1–4	600 (10)	5,400 (90)	760 mS m^{-1}	Figure 12
1–5	600 (10)	7,200 (120)	790 mS m^{-1}	Figure 12
1–6	3,600 (60)	67,500 (1, 125)	410 mS m^{-1}	Figure 12
1–7	600 (10)	2,400 (40)	2020 mS m^{-1}	Figure 11
2–1	240 (4)	2,400 (40)	1 ppm	Figure 12
2–2	240 (4)	2,400 (40)	1 ppm	Figure 11 and 12
2–3	240 (4)	7,200 (120)	1 ppm	Figures 12 and 14

[a]All the experiment have been performed with a flow rate of 2×10^{-4} m^3 s^{-1} (i.e., 12 L min^{-1}). Experiment 1–7 was performed with a pause of 32,700 s between the end of the injection and the beginning of the withdrawal.
[b]The first value is in s, and the value in parenthesis is in min.

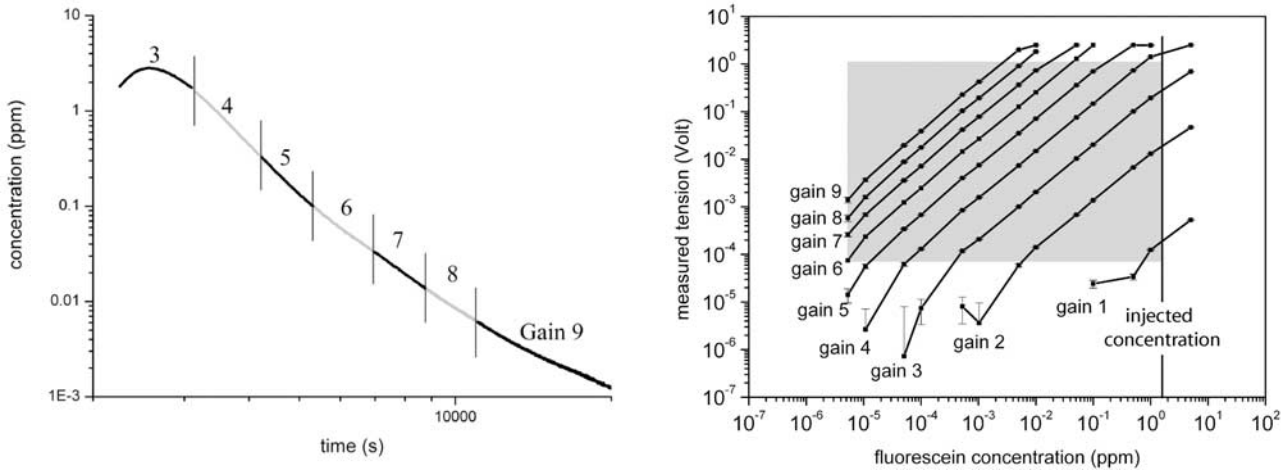

Figure 10. (left) Example of raw BTC. The use of self-adaptive gain allows optimizing the signal-to-noise ratio over more than 5 orders of magnitude from about 100 ppt to 500 ppm in the sea intrusion water. In this figure gain from 3 to 9 is reported. For each of the gains raw data range from 0 to 5 V with a theoretical resolution of 6×10^{-7} V (23 bits) and a measured accuracy during these experiments (taking into account the diverse sources of noise) of about 3×10^{-5} V ($\sim$ 17 bits). (right) Calibration curves for the different gains. The gray zone corresponds to the optimal calibration matrix.

[22] For tracer 1, tracer concentration c is defined as the relative variation of fluid conductivity: $c(t) = (C_{resident} - C(t))/(C_{resident} - C_0)$, where $C(t)$ is the measured fluid conductivity at time t, $C_{resident}$ is the resident water conductivity and C_0 is the initial tracer conductivity. Temperature is measured continuously in the vicinity of the conductivity electrodes. All the conductivity measurements discussed here are values normalized at 20°C. Using conductivity measurements (Figure 12), the temporal range of observation is less than previously published data sets [*Haggerty et al.*, 2001, *Becker and Shapiro*, 2003] that were obtained by the chemical analysis of pumped water at discrete times. The estimated recoveries with tracer 1 vary between 90% and 99% for the experiments with injection durations less than 7200 s. The estimated recovery for the 7200 s and 67500 s injection duration experiments are 85% and 55%, respectively. The apparent decrease of recovery mass is possibly due to the fact that the average concentration decreases with the push duration and therefore the detection limit is attained quicker (relative to the main concentration peak) when the tracer is flushed longer. Note however that for long push duration the tracer may be pushed at distances larger than the packer lengths. Therefore some leakage to the borehole on the side of the packers is possible.

[23] Processing of the tracer 2 data is quite simple as soon as we have the gain-dependent calibration matrix, since the tracer concentration depends linearly on the measured

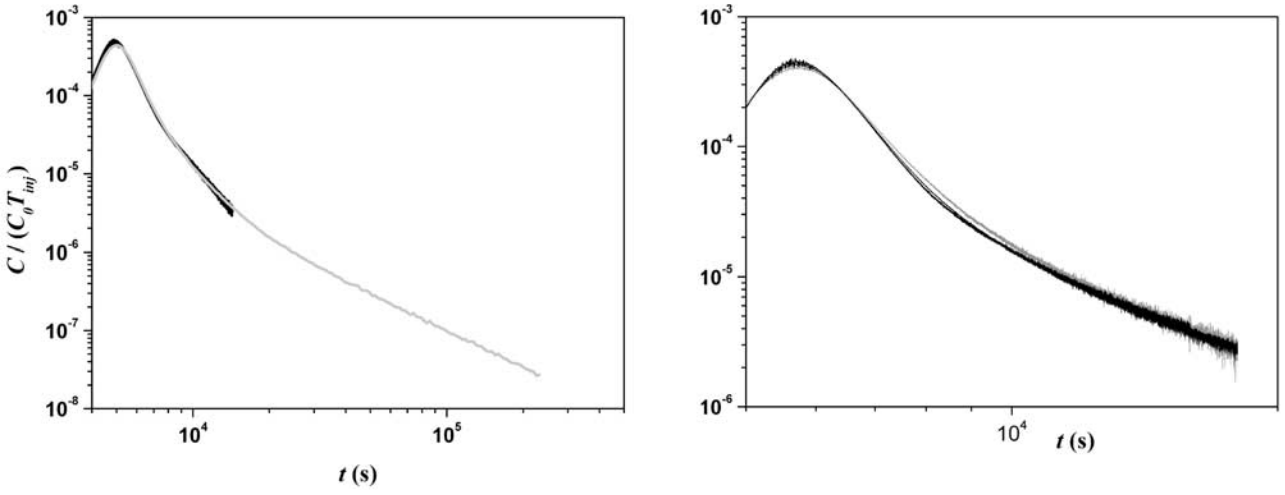

Figure 11. (left) BTC for salinity (test 1–2, black curves) and uranine (experiment 2–2, gray curve) as tracer in well MC2 at depth 94 m. These two tests have been performed at 7 months' interval. (right) BTC for tests 1–1, 1–3 (black curves), and 1–7 (gray curve). These three tests have been performed with the same values for T_{inj} (600 s) and T_{push} (2400 s), but a pause of 32,700 s was added before withdrawal for test 1–7.

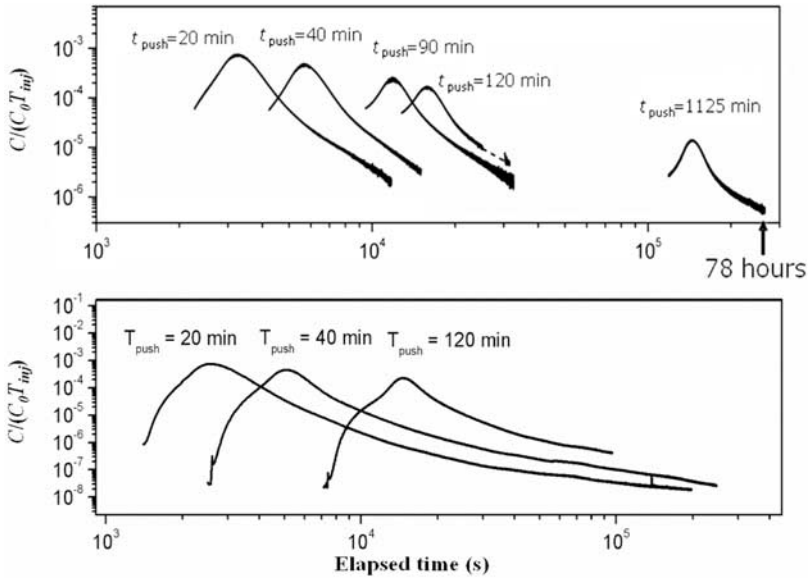

Figure 12. (top) Tracer 1 BTCs for different injection durations: T_{push} = 1200, 2400, 5400, 7200, and 67,500 s (experiment numbers 1–0, 1–3, 1–4, 1–5, and 1–6, respectively; see Table 1). The curves are normalized by c_0T_{inj}, so they integrate to 1. (bottom) Tracer 2 BTCs for T_{push} = 1200, 2400, and 5400 s (experiment numbers 2.1, 2.2, and 2.3, respectively).

uranine concentration (Figure 10). The tracer 2 concentration is given by the relation

$$c = \sum_{i=1}^{9} [(V_i - A_i)B_i]H(V_i),$$

where subscript i refers to the values given when the photomultiplier is set at gain i, V_i is the measured electrical current given by the photomultiplier, A_i and B_i are the coefficients of the calibration curves, and $H(Vi) = 1$ if V_i ranges between the minimal and maximal values defined for the optimal gain i, and $H(V_i) = 0$ otherwise.

[24] Results are displayed in Figure 12. As it was already visible in Figure 11, using tracer 2 (fluorescence measurement) improves strongly the characterization of the tailing for all the push time duration. Measurements are performed over more than 4 orders of magnitude which matches the better resolution obtained by at-surface sampling technique used for example by *Haggerty et al.* [2001]. In terms of data accuracy, the main improvements here, compared to the other published SWIW experiments, are that (1) dispersion, and probably mass transfers, occurring in the tubing, valves and manifolds are avoided, and (2) the time resolution is high (1 data set every 9 s). Furthermore, repeatability of the measurement is rarely performed using conventional at-surface sampling method, because of the great effort required both in terms of manpower and cost. We do so, by repeating tracer test for T_{inj} = 600 s and T_{push} = 2400 s twice. The BTC corresponding to these two similar tests are displayed in Figure 11. The discrepancy between the two BTC is tiny, while the two tests have been performed at 7 months interval.

4.2. Scaling of the Concentration Maximum

[25] If the tracer pulse duration T_{inj} is small enough compared to the advection duration $\tau = 2T_{push} + T_{inj}$, an important property of the SWIW tracing test configuration is that t_{C_max}, the time at which the maximum concentration peak is measured, depends only on the experimental set up (i.e., T_{push}, T_{inj} and Q) and not on the dispersion and mass exchanges properties. We verified this property from numerical simulations [*Le Borgne and Gouze*, 2008, section 4.3]. This is a fundamental difference between SWIW experiments and well-to-well tracer tests. For the later configuration, the peak arrival time can be used to deduce the effective porosity whereas in SWIW tracing experiment, the effective porosity has to be deduced from independent data. Assuming that the tracer does not undergo irreversible mass exchanges with the rock matrix, a linear relation between $t_{C\_\max}$ and τ is expected (Figure 13). Whereas

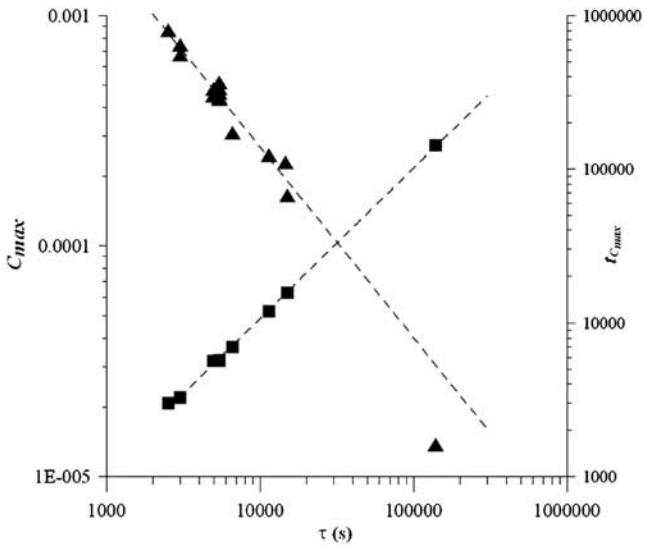

Figure 13. Scaling of C_{max} and t_{Cmax} with the injection duration τ.

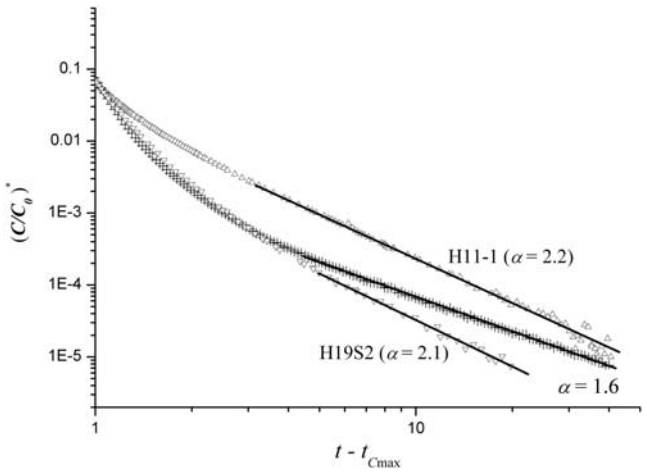

Figure 14. Comparison of the late time slope for the tracer BTC (experiments H11−1 and H19S2) proposed by *Haggerty et al.* [2001] with our results (test 2−3). Concentrations are renormalized in order to have the same maximum value $C_{\max}$.

the scaling of t_{C_max} is useless to identify MIM mass transfers, the scaling of the maximal concentration C_{max} with the advection duration τ may be used to get a first insight into the overall dispersion and to determine non-Fickian behaviors since a deficit of mass at the peak time is expected if BTCs display heavy tailing. Numerical experiments [*Le Borgne and Gouze*, 2008, Figure 7] show that, for SWIW configuration, C_{max} is expected to decrease as a power law of time: $C_{\max} \sim \tau^{-\beta}$(with $\tau \gg T_{inj}$) in the case of the MIM mass transfer model. The value of β is characteristic of the transfer rate distribution in the immobile domain [*Le Borgne and Gouze*, 2008]. The comparison of the measured $C_{\max}\tau$ values with the power law trends shows that a noticeable deviation is observed for the largest injection time (Figure 13). The origin of this lower value of $C_{\max}$ will be discussed by *Le Borgne and Gouze* [2008].

4.3. Late Time Behavior of the BTCs

[26] Many examples of in situ [*Adams and Gelhar*, 1992; *Meigs and Beauheim*, 2001; *Becker and Shapiro*, 2003] and laboratory [*Silliman and Simpson*, 1987; *Berkowitz et al.*, 2000; *Levy and Berkowitz*, 2003] tracer tests display strongly asymmetric BTCs with long tails similar to ours, indicating the occurrence of non-Fickian dispersion processes. Generally, the late time BTC appears to decrease more or less as a power law of time $C(t) \sim t^{-\alpha}$and is explained by the classical MIM mass transfer model. In particular, SWIW experiments have been discussed by *Haggerty et al.* [2001] (WIPP site) and *Becker and Shapiro* [2003]. Both these authors obtained BTC with a late time slope ($-\alpha$) with $\alpha \geq 2$, whereas we observed late time slope that converges to values closer to those expected from the conventional double-porosity model (α = 1.5). While *Haggerty et al.* [2001] interpret their results by MIM mass transfer model, implying that non-Fickian BTC arises from small-scale multirate mass transfers with the immobile domain, *Becker and Shapiro* [2003] proposed that the origin of the observed late time slope is due to large-scale correlations of the velocity field which could be modeled by a stream tube model. However, it must noted that the BTC discussed by *Becker and Shapiro* [2003] is measured over 2 orders of magnitude only, which, as our results indicate, is possibly not sufficient to tackle the asymptotic behavior of the dispersion processes. Conversely, the tracing experiments discussed by *Haggerty et al.* [2001] are more comparable to ours in term of experimental procedure. Yet, two main differences must be pointed out. First, the natural reservoirs in which tracer tests have been performed are noticeably different. The multiscalar heterogeneity described by *Meigs and Beauheim* [2001] for the fractured dolomite investigated at the WIPP site is far more developed than in the Ses Sitjoles test site, which was chosen for its remarkable homogeneity. Second, the experimental protocol of *Meigs and Beauheim* [2001] includes a pause (no flow condition) for duration of about 17 h between the injection and the withdrawal step so that a larger influence of the MIM mass transfers in the overall dispersion is anticipated for the same T_{push} duration. It is then expected that the apparent dispersion close to the maximum concentration peak increases when increasing the pause duration (for the same T_{push} duration) and that the power law tail contribution to the BTC starts at smaller elapsed time. Conversely, the pause should have no effect on the tail log-log slope. We tentatively test this assumption by repeating tracer test 1−3 (T_{inj} = 600 s and T_{push} = 2400 s) but with a pause of 32,700 s (∼9 h). Results are displayed in Figure 11. The expected divergence between the two cases (i.e., without pause and with pause) is detectable, albeit the pause duration was too short to produce large differences.

[27] Figure 14 displays the renormalized BTC for experiment H11−1 and H19S2 (WIPP site) studied by *Haggerty et al.* [2001] and the BTC for experiment MC2_f5 at Ses Sitjoles site. Both H11−1 and H19S2 BTCs display an asymptotic α value close to 2.2, whereas MC2_2.3 BTC (and all the others BTC measured at this depth, see Figure 11) is characterized by an asymptotic value of α close to 1.5. However, it is worth noticing that the first part of the concentration decrease for experiment H19S2 resembles the ones we obtained. If we have had only tracer 1 BTCs, that covers only the part of the late time slope, our data and those from H19S2 would have been apparently similar.

4.4. MIM Mass Transfer Model

[28] The mass balance equation (advection-dispersion equation, ADE) modeling the concentration distribution C_m (**x**,*t*) of single specie in the mobile domain is [*Coats and Smith*, 1964; *Carrera et al.*, 1998; *Haggerty et al.*, 2001; *Berkowitz et al.*, 2002; *Schumer et al.*, 2003]:

$$\phi_m \frac{\partial C_m}{\partial t} = \nabla \cdot (\mathbf{D}\nabla C_m) - \mathbf{q}\nabla C_m - F_{im} \qquad (1)$$

where ϕ_m is the mobile domain porosity, **D** is the dispersion tensor and **q** is the Darcy velocity (or specific discharge); $\mathbf{q} = \phi_m \mathbf{v}$ with **v** the mean pore velocity. In equation (1), F_{im} (**x**,t) is the sink-source term that represents the volumetric mass flux (M L^{-3} T^{-1}) of solute transferred from the mobile zone to the immobile zone $F_{im} = \phi_{im}\partial C_{im}/\partial t$, with C_{im}(**x**,*t*) the averaged solute concentration of the immobile domain at coordinate **x**. More precisely, F_{im} (**x**,*t*) is the mass flux from the mobile to the immobile zone per unit volume of aquifer (V_{tot}). With the adequate boundary and initial con-

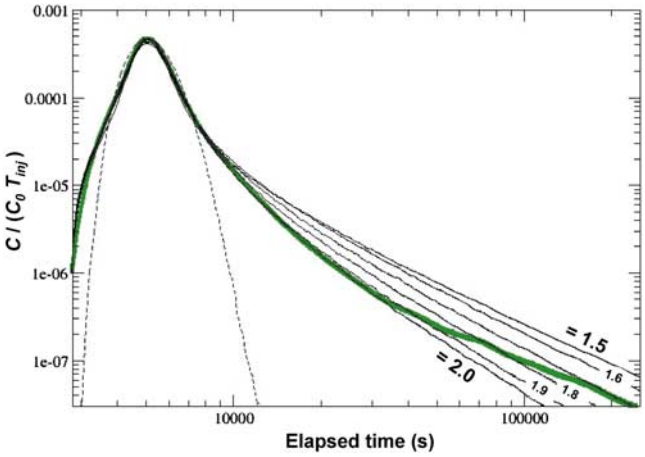

Figure 15. Best fits of tracer test 2.2 by the MIM mass transfer rate model for α ranging from 1.5 to 2. The best fit using ADE is given for comparison (dotted curve).

ditions, equation (1) expresses the mass conservation balance in time and space. The immobile domain corresponds to portions of aquifer where flow is negligible compared to what exists in the mobile domain; it then includes the fraction of solid containing connected microporosity or intergrains porosity as well as stagnant water in dead ends [*Haggerty and Gorelick*, 1995]. If the mean microporosity of the immobile domain is ϕ_{im}', then $\phi_{im} = (1 - \phi_m)\phi_{im}'$. Note that in the most general case, ϕ_{im} and ϕ_m are distributed values, but we will consider here that this values are constants over the volume of rock visited by the tracer. For linear mass transfer processes, such as diffusive mass transfer, F_{im} may be expressed as a convolution product [*Carrera et al.*, 1998; *Haggerty et al.*, 2000; *Dentz and Berkowitz*, 2003]:

$$F_{im}(\mathbf{x},t) = \int_{t'=0}^{t} \frac{\partial C_m(\mathbf{x},t-t')}{\partial t} G(t')dt' = \frac{\partial C_m(\mathbf{x},t)}{\partial t} * G(\mathbf{x},t) \quad (2)$$

where notation '*' refers to the convolution product, G [T^{-1}] is the memory function which contains all the information about the mass transfer process, the geometry and the volume fraction of the immobile domain and its accessibility to the tracer particle issued from the mobile domain. The memory function $G(t)$ denotes the probability density that a tracer particle entering the immobile zone at $t = 0$ remains in it at time t.

[29] For weakly variable velocity field, such as implied by the Fickian dispersion model in the mobile domain, an approximation of the tracer concentration for late time C_{m-lt} (t) is given by *Haggerty et al.* [2000] for C_m $(\mathbf{x},t = 0) = 0$:

$$C_{m-lt} \approx -t_{ad} C_0 t_{inj} \frac{\partial G}{\partial t}, t_{ad} \ll t \ll t_{res} \quad (3)$$

where C_0 is the pulse concentration at $t = 0$ and t_{inj} the duration of the pulse and t_{ad} is the average advective residence time of the solute moving from the input to the an observation location $\mathbf{x}_{obs}$: $t_{ad} = \mathbf{x}_{obs}/\mathbf{v}$. Indeed, at late time, i.e., as the concentration pulse has moved far past the observation location $\mathbf{x}_{obs}$ ($t \gg t_{ad}$), concentration in the mobile domain is almost independent of the hydrodynamic dispersion: $\mathbf{D}\nabla C_m \ll C_m$. It is then obvious from (3) that the occurrence of power law tailed BTC (C_{m-lt} $(t) \sim t^{-\alpha}$) requires $G(t)$ being a power law distribution scaling as $G(t) \sim t^{-\alpha+1}$. This behavior would persist infinitely if the tracer could access to larger diffusion paths (i.e., longer residence time) as time increases. This could happen in a true fractal system. However, in natural porous media, a maximum diffusion length, corresponding to the larger size structures, is expected, and the power law decrease persists until t_{res} which denotes the maximum residence time in the mobile domain. The value of t_{res}, that corresponds to the time when the concentration decrease abruptly (i.e., α tends to ∞), is generally not measured on BTCs because it would require larger acquisition time and better measurement resolution than it is technologically possible. Figure 15 displays the best fit obtained for different power law rate distributions including the conventional double-porosity model ($\alpha = 1.5$). It is important to note that although we have no information to force the value of t_{res} in the model (we can only affirm that t_{res} is larger than the experiment duration, i.e., 3×10^5 s), its influence on the data fitting is negligible. Results show that none of the multirate diffusion MIM models can explain the entire shape of the BTC (tracer 2). More specifically, the progressive change of the late time BTC slope from $\alpha = 2$ to $\alpha = 1.5$ cannot be reproduced by the classical multirate MIM model. The multi rate diffusion can be conceptualized by assuming that the immobile domain is formed of an assemblage of spheres or slabs of given diffusion rate. The conventional double-porosity model ($\alpha = 1.5$) is obtained assuming a single sphere size distribution [*Carrera et al.*, 1998]. Conversely, for $\alpha = n$ (with $n > 2$), it can be shown that the equivalent sphere radius distribution scales as R^{3-2n}, with R the sphere radius. Then, for $\alpha = 2$, the diffusion is suppose to take place in an assemblage of spheres characterized by a distribution of sphere radius scaling as $1/R$. The occurrence of two slopes, or more generally of nonlinear log(C) − log(t) BTC at large time, requires involving MIM mass transfers involving non−power law memory function, or in other words, non−power law diffusion rate distribution. In a companion paper [*Le Borgne and Gouze*, 2008] this data will be studied in the frame of the constant time random walk approach, and it will be shown that a two stages heterogeneity model can explain the observed BTC behavior.

5. Summary and Conclusions

[30] The set of tracing experiments presented in this paper produces an accurate database for measuring non-Fickian dispersion processes induced by the presence of diffusion in immobile zones in porous media. The use of SWIW tracing configuration allows us performing a large set of tracing tests, with distinctly different investigation volumes, in a relatively short period of time. Then, dispersion modeling [see *Le Borgne and Gouze*, 2008] can be constrained not only by fitting dispersion parameter for a single BTC, but taking into account scale effects. Using radial convergent/divergent configuration permits to focus on the longitudinal dispersion because transversal dispersion is not expected to affect the breakthrough curve for this configuration.

[31] The new equipment developed for these tracing experiments allows controlling the shape of the injection

pulse (i.e., rectangular injection, with very small durations so that it approaches dirac injection). For both tracers, measurements are performed directly in the pumping chamber, minimizing strongly the dispersion in the tubing which superimposes onto the reservoir dispersion when measuring the tracer concentration with surface equipments. Furthermore, measurements are performed continuously: one data every 9 s, each of them representing the average of 30 data acquisitions. Finally, to overcome flow rate variations induced by fluctuations of the borehole skin effect, for instance because of fine particles accumulation in the well annulus during withdrawal phase, the flow rate is automatically maintained constant whatever the pressure fluctuations are.

[32] The combination of two tracers, for which measurement techniques are distinct (conductivity measurement and optical measurement), allows us verifying the pertinence of the experimental procedure. More specifically, this methodology is implemented for verifying that the tracers behave as passive tracers and that density effects do not induce perturbations on the BTCs. The use of fluorescent dye as tracer (tracer 2) in seawater has proved to be practical and allows accurate measurements up to 5 orders of magnitude on the concentration during the recovery phase. Mass recovery for tracer 2 is always close to 1 showing that (1) tracer is chemically conservative; (2) no mass loss due to leak along the packers is encountered during the tracer tests except for test 1–6 (T_{push} = 67500 s) for which it is expected that the maximal tracer penetration distance exceeds the length of the packers; (3) the tracer tests allow measuring the almost complete dispersion behavior and (4) the tracer experiment in SWIW mode permits to cancel reversible dispersion, i.e., the effect of long-range velocity correlation that could exist because of preferential flow path.

[33] Recorded BTCs do not show a linear late time log-log slope as it is predicted by the conventional MIM mass transfer model. The first part of the late time slope displays a gradual decrease of the concentration which could have been fitted almost satisfactory with a MIM model characterized by $\alpha = 2$. Indeed, using the tracer 1 data only, this misinterpretation could have been done. The second part of the late time BTC shows a clear asymptotic behavior toward $\alpha = 1.5$. This seems to indicate that a double-porosity behavior take place when the tracer visit immobile domain a large size and/or low diffusivity, or in other words, that a fraction of the immobile domain is made of homogeneous large size and/or low diffusivity structure. This would explain the departure from the linear relation between log ($C_{\max}$) and log (τ) for large values of τ (Figure 13). This assumption will be studied in a companion paper *Le Borgne and Gouze* [2008]. Determining the origin of this anomalous behavior, compared to the conventional MIM mass transfer model, requires a better characterization of the immobile domain characteristics including the diffusivity heterogeneity and the accessibility of the immobile domain to the tracer moving in the mobile domain. A simple observation of the microstructures (e.g., Figures 4 and 6) shows that modeling the complexity of the diffusion path by a simple power law distribution of diffusion rates is probably unrealistic. This investigation will be presented in a forthcoming paper.

[34] **Acknowledgments.** This work was funded by the European project "ALIANCE" (Advanced Logging Investigations in Coastal Environments, contract EKV-2001-00039). All the members of the ALIANCE team are gratefully acknowledged for their support, as well as C. Gonzalez and A. Baron of the Ministry of Environment of the Balearic Islands Government.

References

Adams, A. E., and L. W. Gelhar (1992), Field study of dispersion in a heterogeneous aquifer: 2. Spatial moments analysis, *Water Resour. Res.*, *28*(12), 3293–3307.

Becker, M. W., and A. M. Shapiro (2003), Interpreting tracer breakthrough tailing from different forced-gradient tracer experiment configurations in fractured bedrock, *Water Resour. Res.*, *39*(1), 1024, doi:10.1029/2001WR001190.

Benson, D. A., R. Schumer, M. M. Meerschaert, and S. W. Wheatcraft (2001), Fractional dispersion, Lévy motion, and the MADE tracer tests, *Transp. Porous Media*, *42*, 211–240, doi:10.1023/A:1006733002131.

Berkowitz, B., H. Scher, and S. E. Silliman (2000), Anomalous transport in laboratory-scale, heterogeneous porous media, *Water Resour. Res.*, *36*(1), 149–158, doi:10.1029/1999WR900295.

Berkowitz, B., J. Klafter, R. Metzler, and H. Scher (2002), Physical pictures of transport in heterogeneous media: Advection-dispersion, random-walk, and fractional derivative formulations, *Water Resour. Res.*, *38*(10), 1191, doi:10.1029/2001WR001030.

Bernard, D., Ø. Nielsen, L. Salvo, and P. Cloetens (2005), Permeability assessment by 3D interdendritic flow simulations on microtomography mappings of Al-Cu alloys, *Mater. Sci. Eng. A*, *392*(1–2), 112–120, doi:10.1016/j.msea.2004.09.004.

Carrera, J., X. Sánchez-Vila, I. Benet, A. Medina, G. Galarza, and J. Gimera (1998), On matrix diffusion: Formulations, solution methods and qualitative effects, *Hydrogeol. J.*, *6*(1), 178–190, doi:10.1007/s100400050143.

Coats, K. H., and B. D. Smith (1964), Dead end pore volume and dispersion in porous media, *SPEJ Soc. Pet. Eng. J.*, *4*, 73–84, doi:10.2118/647-PA.

Dentz, M., and B. Berkowitz (2003), Transport behavior of a passive solute in continuous time random walks and multirate mass transfer, *Water Resour. Res.*, *39*(5), 1111, doi:10.1029/2001WR001163.

Gelhar, L. W., and M. A. Collins (1971), General analysis of longitudinal dispersion in nonuniform flow, *Water Resour. Res.*, *7*(6), 1511–1521, doi:10.1029/WR007i006p01511.

Gylling, B., L. Moreno, and I. Neretnieks (1999), The Channel Network Model—A tool for transport simulation in fractured media, *Ground Water*, *37*(3), 367–375, doi:10.1111/j.1745-6584.1999.tb01113.x.

Haggerty, R., and S. M. Gorelick (1995), Multiple-rate mass transfer for modeling diffusion and surface reactions in media with pore-scale heterogeneity, *Water Resour. Res.*, *31*(10), 2383–2400.

Haggerty, R., S. A. McKenna, and L. C. Meigs (2000), On the late-time behavior of tracer test breakthrough curves, *Water Resour. Res.*, *36*(12), 3467–3480, doi:10.1029/2000WR900214.

Haggerty, R. S., S. W. Fleming, L. C. Meigs, and S. A. McKenna (2001), Tracer tests in a fractured dolomite: 2. Analysis of mass transfer in single-well injection-withdrawal tests, *Water Resour. Res.*, *37*(5), 1129–1142, doi:10.1029/2000WR900334.

Jaeggi, D. (2006), Multiscalar porosity structure of a miocene reefal carbonate complex, Ph.D. dissertation, Naturwiss., Eidg. Tech. Hochsch. ETH Zurich, Zurich, Switzerland.

Khrapitchev, A. A., and P. T. Callaghan (2003), Reversible and irreversible dispersion in a porous medium, *Phys. Fluids*, *15*, 2649–2660, doi:10.1063/1.1596914.

Le Borgne, T., and P. Gouze (2008), Non-Fickian dispersion in porous media: 2. Model validation from measurements at different scales, *Water Resour. Res.*, *44*, W06427, doi:10.1029/2007WR006279.

Le Borgne, T., J.-R. de Dreuzy, P. Davy, and O. Bour (2007), Characterization of the velocity field organization in heterogeneous media by conditional correlation, *Water Resour. Res.*, *43*, W02419, doi:10.1029/2006WR004875.

Levy, M., and B. Berkowitz (2003), Measurement and analysis of non-Fickian dispersion in heterogeneous porous media, *J. Contam. Hydrol.*, *64*(3–4), 203–226, doi:10.1016/S0169-7722(02)00204-8.

Lods, G., and P. Gouze (2004), WTFM, a software for well tests analysis in fractured media combining fractional flow with double porosity and leakance, *Comput. Geosci.*, *30*, 937–947, doi:10.1016/j.cageo.2004.06.003.

Meigs, L. C., and R. L. Beauheim (2001), Tracer tests in fractured dolomite: 1. Experimental design and observed tracer recoveries, *Water Resour. Res.*, *37*(5), 1113–1128, doi:10.1029/2000WR900335.

Noiriel, C., D. Bernard, P. Gouze, and X. Thibault (2005), Hydraulic properties and microgeometry evolution in the course of limestone dissolution by CO_2-enriched water, *Oil Gas Sci. Technol.*, *60*(1), 177–192, doi:10.2516/ogst:2005011.

Pomar, L. W. C., and C. Ward (1999), Reservoir-scale hetrogeneity in depositional packages and diagenetic patterns on a reef-rimmed platform, Upper Miocene, Mallorca, Spain, *AAPG Bull.*, *83*, 1759–1773.

Schumer, R., D. A. Benson, M. M. Meerschaert, and B. Baeumer (2003), Fractal mobile/immobile solute transport, *Water Resour. Res.*, *39*(10), 1296, doi:10.1029/2003WR002141.

Silliman, S. E., and E. S. Simpson (1987), Laboratory evidence of the scale effect in dispersion of solutes in porous media, *Water Resour. Res.*, *23*(8), 1667–1673, doi:10.1029/WR023i008p01667.

Tenchine, S., and P. Gouze (2005), Density contrast effects on tracer dispersion in variable aperture fractures, *Adv. Water Resour.*, *28*(3), 273–289, doi:10.1016/j.advwatres.2004.10.009.

Tsang, Y. W. (1995), Study of alternative tracer tests in characterizing transport in fractured rocks, *Geophys. Res. Lett.*, *22*(11), 1421–1424, doi:10.1029/95GL01093.

P. Gouze, R. Leprovost, G. Lods, P. Pezard, and T. Poidras, Géosciences, UMR 5243, Université de Montpellier 2, CNRS, F-5243, Montpellier, France.

T. Le Borgne, Géosciences Rennes, UMR 6118, Université de Rennes 1, CNRS, F-35042, Rennes, France. (tanguy.le-borgne@univ.rennes1.fr)